


# A Compact Mid-Wave Infrared Imager System With Real-Time Target Detection and Tracking

Xuan Deng , Yueming Wang , Daogang He, Guicheng Han, Tianru Xue , Yifan Hao, Xiaoqiong Zhuang, Jun Liu, Changxing Zhang, and Shengwei Wang

**Abstract**—The mid-wave infrared imager has stronger transmission ability than the visible near-infrared imager, which can effectively overcome the limitation of the low-visibility climate on the image acquisition timeliness. Moreover, it is more conducive to the detection of long-distance small target. However, few infrared imager systems track the long-distance aerial target while detecting it in real-time. Meanwhile, conventional optical structures for long-distance imaging are cumbersome and bulky. Thus, the significant challenge to solve this problem is how to design a lightweight infrared imaging system for the detection of long-distance infrared small targets over complex scenes. In this article, the basic principle and design features of a compact mid-wave infrared imager system are detailed. The optical system has an ingenious design, compact structure, low power consumption, lightweight, and low installation cost. Simultaneously, an improved features from the accelerated segment test (IFAST) target detection algorithm is proposed, which is verified by comparative experiment, showing good robustness, and stability for infrared small target detection. Combining IFAST with two-dimensional turntable can realize the requirement of real-time object tracking and two filed imaging experiments were carried out. The results demonstrate the robustness and stability of the imager system in detecting and tracking infrared small targets, which can provide a reference for the design of compact mid-wave infrared instruments for similar applications.

**Index Terms**—Compact optical design, mid-wave infrared imager system, real-time tracking, small target detection.

## I. INTRODUCTION

IT IS well known that target detection and tracking have a wide range of applications in such areas as remote sensing, surveillance, early warning, aerospace, alert search, data classification, and so on [1]–[5]. Any object with a temperature greater than absolute zero Kelvin emits radiation with a wavelength distribution. The radiative energy depends on the temperature

Manuscript received 6 April 2022; revised 27 June 2022 and 13 July 2022; accepted 16 July 2022. Date of publication 19 July 2022; date of current version 4 August 2022. (Corresponding author: Yueming Wang.)

Xuan Deng, Yueming Wang, Tianru Xue, and Yifan Hao are with the Key Laboratory of Space Active Opto-Electronics Technology, the Shanghai Institute of Technical Physics, Chinese Academy of Sciences, Shanghai 200083, China, and also with the University of Chinese Academy of Sciences, Beijing 100049, China (e-mail: dengxuan@mail.sitp.ac.cn; wangym@mail.sitp.ac.cn; xuetianru@mail.sitp.ac.cn; haoyifan@mail.sitp.ac.cn).

Daogang He, Guicheng Han, Xiaoqiong Zhuang, Jun Liu, Changxing Zhang, and Shengwei Wang are with the Key Laboratory of Space Active Opto-Electronics Technology, the Shanghai Institute of Technical Physics, Chinese Academy of Sciences, Shanghai 200083, China (e-mail: hedaogang@mail.sitp.ac.cn; hgc@mail.sitp.ac.cn; kelly\_3839@sina.com; liujun@mail.sitp.ac.cn; zhangchangxing@mail.sitp.ac.cn; wswpp163@163.com).

Digital Object Identifier 10.1109/JSTARS.2022.3192311

of the object and its wavelength distribution by Planck radiation law [6]. Real objects are rarely blackbodies in practice. The amount of energy radiated by an object largely depends on the material properties of the surface [7]. Depending on the object material, thickness, and the radiation wavelength, part of the radiation may pass through the object or be transmitted. The transmission coefficient can vary between 0 and 1, while the emissivity of radiators in nature is less than 1. The object absorbs the remaining energy and its temperature is increased, making infrared imaging technology one of the most important detection methods for target detection and tracking. The “atmospheric window” includes the mid-wave infrared band with a wavelength of 3–5  $\mu\text{m}$  [8]. In this band, the atmosphere can transmit many components of infrared radiation, so it is often adopted as the main window for infrared thermal imaging. Compared with the visible near-infrared, the mid-wave infrared has a longer wavelength and has a stronger ability to penetrate fog, rain, snow, and smoke. It is not easily affected by haze scattering and can overcome the limitation of low-visibility climate on the timeliness of remote sensing image acquisition. In addition, mid-wave infrared has a longer range in the field of aerial target detection, which is more conducive to the detection of long-distance small target. Different temperature targets have higher thermal contrast in the mid-wave infrared band, making it easier to distinguish between them. The corresponding wavelength of the 600–1000 Kelvin object radiation power peak is the mid-wave, which makes the mid-wave infrared have superior thermal infrared high-temperature object monitoring ability [9].

Infrared imaging systems operate in the infrared band with passive noncontact and are not limited by day and night. The infrared imaging system is sensitive to the thermal radiation of the target, has strong resistance to electronic interference, and has good concealment. It can recognize camouflage in the presence of strong electronic interference. The infrared imaging system has strong detection and recognition ability for stealth aircraft, drones, and other hidden target or target under strong light interference, which is more suitable for high-precision observation than radar [10]. Meanwhile, the infrared imaging system can collaborate with radar and radio to fill the blind spot of radar [11], [12]. Therefore, with the outstanding advantages of good imaging quality, high detection accuracy, strong anti-interference ability, and all-day work, the infrared imaging system has become one of the core equipment for target acquisition and tracking in the photoelectric tracking and

aiming system. Its performance will directly affect the capture capability and tracking accuracy of the tracking and aiming system.

With the advancement of detector level and infrared imaging technology, achieving a large field of view, high resolution, compactness, and lightweight has gradually become the mainstream direction for infrared camera development. Beach [13] designed an optical system working in the mid-wave infrared band using the multiple refraction and reflection approach to improve its compactness for optomechanical efficiency. Hong *et al.* [14] used a scanning oscillating mirror to design a zoom infrared optical system operating in the mid-wave and long-wave range. Sanson and Cornell [15] fabricated a mid-wave infrared thermal imaging system with a large zoom system to increase the field of view. The DMC modular digital aerial camera launched by Z/I Imaging was composed of multiple small cameras to obtain a wide field of view data [16]. High-resolution images were finally obtained after data fusion and registration processing. The A3 digital camera from Israel employs a large area array sweep in exchange for a large field of view imaging [17]. He and Zhao [18] developed an integrated mid-wave infrared optical system with an axis-zoom of four fields of view. However, the wide-field imager system produced by splicing multiple cameras has many devices and complicated operations. Most of the infrared imager systems for acquiring multiview data images by sweeping a wide range are bulky and heavy. Multiview image data is difficult to achieve with an imaging system that utilizes multiple zoom ratios to obtain a wide field of view. As a result, the development direction for the new generation of infrared photoelectric equipment is to realize the lightweight of the system and have the application requirements of long focal length and multiple fields of view.

Tracking after detection is a common target acquisition strategy [19]. At present, most of the real-time target tracking is to track the moving target in the captured dataset or video in a fixed background, with only a few instances of tracking while detecting. When the movement trajectory of the captured target does not traverse the entire field of view, the movement time of the target in the field of view and the captured target information will be greatly reduced. During the movement of the target, once it leaves the limited field of view of the imaging system, it will be impossible to track the target, and the target capture will be lost. Thus, how to increase the dwell time of the target in the imaging field of view is one of the major challenges in target tracking. Most of the real-time target tracking stays in the dataset simulation, and there are relatively few practical applications for real-time tracking while collecting in the field test. Nevertheless, in practical applications, ensuring the real-time performance of target tracking has urgent application requirements and important practical value. Simultaneously, target detection accuracy and stability play a decisive role in the execution and decision-making of the target tracking [20], [21]. Small infrared targets are detected using the infrared radiation properties that can locate target in complex environment, such as aircraft in clouds, aircraft in complex terrain, and so on [22]–[24]. The background of the target occupies most of the image due to the influence of long-distance imaging, resulting in many infrared

targets with a small scale and low signal-to-noise ratio [25]. The lack of target shape and texture information also makes target detection difficult [26], [27]. Although many detection algorithms for these problems have been presented in related works, there are still some difficulties in the detection of infrared small targets in complex environments.

Traditional spatial domain-based algorithms rely on the estimation of background information, including the Robinson–Guard filter based on pixel aggregation degree estimation (ERG) [28], two-dimensional (2-D) minimum mean square [29], the nonlinear filter based on background estimation [30], the Top-Hat filter [31], Max-mean/Max-median filter [32], and Bilateral filter [33]. However, due to the lack of noise suppression ability, they are vulnerable to the influence of background and noise in complex environments, and the performance reliability is unstable.

Furthermore, numerous transform domain-based methods were proposed. The image is transformed from the spatial domain to the corresponding domain by a specific transformation. The classical frequency domain filter combines the frequency domain characteristics of the image to suppress the background, including the ideal high-pass filter [34], Butterworth high-pass filter [35], and so on. The image background has a lower radiation intensity than the target, and the gray value of the target and its surrounding is not continuous. Accordingly, Boccignone *et al.* [36] introduced wavelet transform to infrared small-target detection. It is suggested to use the wavelet transform to separate the image background (low-frequency component) and target (high-frequency component) to improve the detection effect. Luo and Wu [37] created a wavelet decomposition model based on directional dispersion. Wang and Tang [38] combined wavelet packet with higher-order statistics (WPT-HOS). In contrast to the spatial domain-based algorithms, the transform domain-based algorithms have high computational complexity, and it is easy to mistake the isolated noise as the target.

In infrared small target detection, there is an obvious gray difference between a small target and its background neighborhood. Hence, some theoretical mechanisms in the human visual system (HVS) are also applied to infrared small target detection. In 2014, Chen *et al.* [39] first proposed the local contrast method (LCM). Whereas, the LCM algorithm has the problems of block effect and centroid localization error in the target saliency map. Han *et al.* [40] developed an enhanced detection method for local contrast measurement, which introduced the problem of smoothing small targets. Chen and Xin [41] designed a local saliency map (LSM) for local self-similar computation utilizing the weighted uniform properties of surrounding regions. To solve the defect of the block effect of the LCM algorithm, a multiscale patch-based contrast measure (MPCM) appeared [42]. Qin and Li [43] presented a novel local contrast measure method to suppress the complex background in infrared images. Han *et al.* [44] developed a relative local contrast measure (RLCM) for various scales. Liu *et al.* [45] proposed a novel IR small target detection method utilizing halo structure prior (HSP) based LCM (HSPLCM). In addition, some algorithms also used the weighted technique to increase the algorithm

performance, like weighted local contrast measure (WLCM) [46], weighted strengthened local contrast measure [47], weighted local difference measure [48], and homogeneity-WLCM [49]. Target detection algorithms based on HVS are essentially suitable for scenes with higher target intensity and obvious gray differences with the surrounding background neighborhood.

The reconstruction algorithm of the low-rank sparse matrix uses the difference between the target noise and the background to recover it. In the infrared image, the target has sparse features while the background has low-rank characteristics [50]. The infrared patch-image model (IPI) is a representative of these methods [51]. Conversely, IPI does not consider the infrared image background as a more complex heterogeneous background. Dai *et al.* [52] adopted the partial sum of singular values to constrain the low-rank background patch-image and designed a non-negative infrared patch-image model to replace the fixed weighting parameters (NIPPS). Yang *et al.* [53] presented an integrated target saliency measure based on local and nonlocal spatial information. Dai and Wu [54] employed a reweighted infrared patch-tensor model with both nonlocal and local priors for single-frame small target detection (RIPT). The reconstruction algorithm has many applications and good recognition effects, while it has high complexity and poor real-time performance [55].

In response to the aforementioned needs and challenges raise, this article proposes a comprehensive set of mid-wave infrared imaging systems. The real-time tracking function of the target is realized through the strategy of combining the improved features from the accelerated segment test (IFAST) target detection algorithm with the 2-D turntable, which is based on a compact structure and lightweight.

The contributions of this article can be summarized as follows.

- 1) A catadioptric optical design scheme employing a telephoto lens to realize a compact mid-wave infrared imager system is proposed. The combination of a small aperture camera and a 2-D turntable is selected to achieve a wide range of rotation to increase the total field of view for gaze imaging. Meanwhile, the shell adopts 3-D printing technology to significantly reduce the weight of the camera. This not only meets the needs of long-distance and large-scale imaging but also of a compact and lightweight system.
- 2) We proposed an IFAST target detection algorithm and combined it with 2-D turntable to realize target tracking. According to the properties of infrared small targets and noise, the algorithm eliminates as much noise and complex environmental background information as possible. The reliable target pixels are attained through an adaptive threshold to realize the detection of infrared small target. Concurrently, the pitch and yaw directions of the imager system are adjusted according to the output result of the target detection algorithm to maintain real-time tracking of the detected target.
- 3) The mid-wave infrared imaging system is tested in the real field test after the whole machine is installed and adjusted. Experiments for real-time observation and

TABLE I  
MAIN PERFORMANCE PARAMETERS OF THE INSTRUMENT

Parameter	Performance	
Spectral Range	3.7–4.8 $\mu\text{m}$	
Array Size	640×512	
Focal Length	150 mm	
Pixel Pitch	15 $\mu\text{m}$	
Instantaneous Field of View (IFOV)	0.1 mrad	
Field of View (FOV)	3.66°×2.93°	
Average Power	30 W	
Weight	7.2 kg	
Observation Range	Yaw Range	-180°~ +180°
Observation Range	Pitch Range	0°~ +90°

tracking of long-distance flying target are carried out. Through these experiments, the performance and function of the instrument are verified, which provides a reference for further applications in the future.

The rest of this article is organized as follows. In Section II, the general design of the compact and lightweight mid-wave infrared imager system is described in detail. Section III introduces small target detection approach and real-time target tracking strategy. Section IV gives comparison results of IFAST with other algorithms in infrared small target detection, as well as the experimental findings of the imager system in outfield tests. Finally, Section V concludes this article.

## II. GENERAL DESIGN

In this article, the basic principles and design features of a compact mid-wave infrared imager system are detailed, mainly used to observe long-distance flying target in the air. The mid-wave infrared imager system can obtain infrared images and ensure continuous work across the day and night. At the same time, it can realize staring imaging or scanning imaging of a designated area in the air. The main performance parameters of the instrument are shown in Table I. The mid-wave infrared imager system operates in the wavelength range of 3.7–4.8  $\mu\text{m}$ .

### A. System Composition

The mid-wave infrared imager system consists of two parts: an infrared photoelectric system and an electric control box. Its appearance drawing is displayed in Fig. 1. A layer of high emissivity aluminum film is attached to the outer surface of the photoelectric system to minimize the influence of the temperature increase on the photoelectric system caused by the long-term sunlight exposure. The total weight is 7.2 kg, with the photoelectric system weighing 5.5 kg and the control box weighing 1.7 kg.

The infrared photoelectric system includes an infrared camera, a 2-D sweeping mechanism, a focusing mechanism, and other components. The infrared camera includes an optical

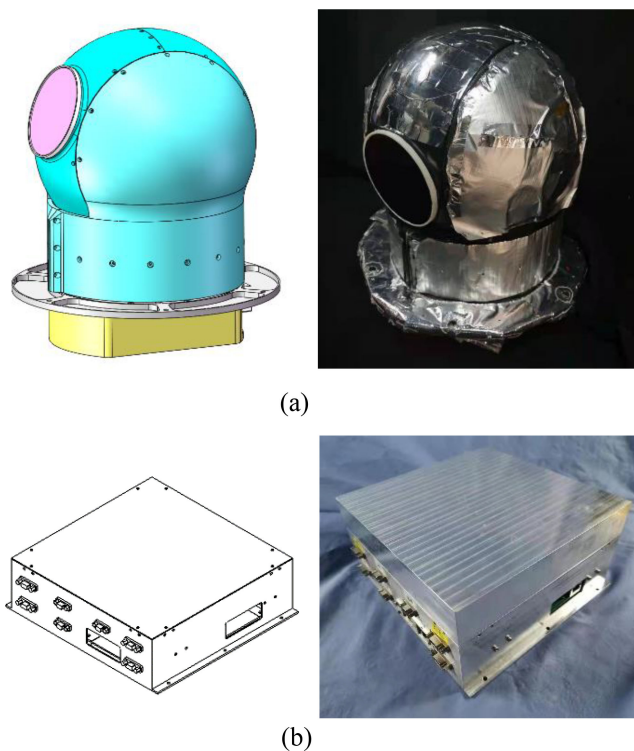


Fig. 1. Appearance drawing of mid-wave infrared imager system. The left side is the original design drawing, and the right side is the physical drawing after installation. (a) Appearance drawing of the infrared photoelectric system. (b) Appearance drawing of the control box.

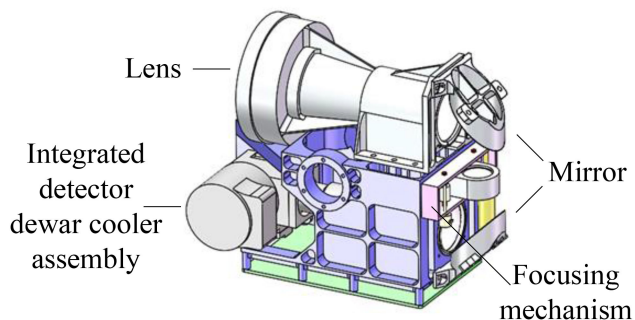


Fig. 2. Internal structure diagram.

system, an integrated detector Dewar cooler assembly, and an imaging electronics module. A compact structure is designed to strictly limit the size and weight of the internal structural components and the optical path is folded by a reflector so that the entire optomechanical component can be covered by a circle. The center of rotation of the optical assembly is fixed at the geometric center. A focusing mechanism is added inside the optical assembly for imaging at different temperatures. The structure of the internal components is presented in Fig. 2. A small stepping motor is installed on the focusing bracket and screwed to the slider. On the upper part of the slider, an optical lens seat is installed and two parallel linear bearings are installed on both sides of the motor. The other side is equipped with a resistive encoder as the position feedback of the kinematic mechanism.

The interior of the electric control box comprises various functional modules such as a power supply, thermal control, monitoring, and recorder. Vibration-sensitive devices are structurally and electronically reinforced. The infrared photoelectric system and the control box are connected by cables. In general, the signal line and its return line in the cable using twisted pairs and shielding, and correspond one-to-one with the connector contacts. The cable joints are reinforced, and the corresponding cables are bound and fixed.

### B. Optical Design

Typical structures of optical systems include reflective systems, transmissive (refractive) systems, and catadioptric systems.

Reflective systems are best suited for applications with high F numbers and small fields of view. Such systems can efficiently compress the optical path length, making the system size much smaller than the system focal length. Typical reflective systems include Newton's system [56], Casarian system [57], and Gregorian system [58].

The transmissive system can achieve a large field of view, which is appropriate for the application requirements of low F number and large field of view [59]. The transmission telephoto system mostly employs a telephoto objective lens to shorten the length of the optical system, i.e., the length of the lens barrel [60]. The ratio of the length of the optical system to the focal length is called the telephoto ratio, which is an important indicator of the telephoto objective. The telephoto ratio of the transmission system is restricted by the angle of view and the relative aperture. When the imaging system adopts an aspherical mirror for primary refraction, the limit of the telephoto ratio is about 0.8 [61]. To reduce the telephoto ratio, more aspheric mirrors or glasses with special relative partial dispersion must be added. This not only increases the cost but also increases the difficulty of installation. The telephoto ratio will be hard to reduce if secondary refraction imaging is applied. Therefore, using refraction imaging systems to meet the application requirements of searching and tracking infrared optical systems is difficult.

The catadioptric system is typically composed of a reflective objective lens and a transmissive correction lens group. It combines the advantages of the reflective system with the large aperture, compressed optical path, and strong correction capability of the transmissive system [62]. By positioning a correction lens in front or rear of the reflection system, the aberration correction capability, and the field of view can be enlarged [63]. Classic catadioptric structures include the Schmidt system, the Makesutov system, and the Mangkin refractor. Among them, the Makesutov system and Mangkin refractor use spherical surfaces, which can greatly simplify the processing.

According to the abovementioned analysis, the optical path structure can be of the transmission type because the optical aperture of the mid-wave infrared imager system is small and the spectral bandwidth of the system is not too wide. Since the working spectrum of the system is 3.7–4.8  $\mu\text{m}$  in the infrared band, silicon and germanium can be selected as the material of the lens group. The pupil adjustment and aberration

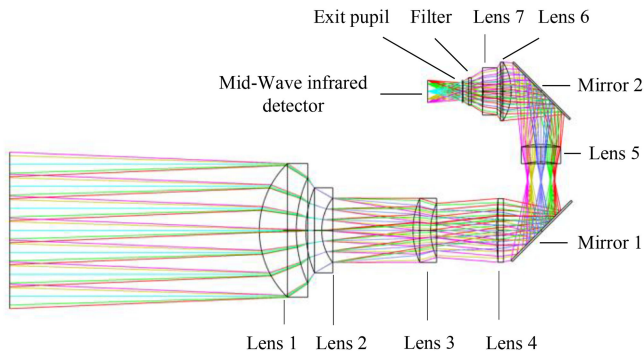


Fig. 3. Ray trace of the mid-wave infrared optical system.

correction are performed by optimizing the surface shape and mirror spacing to achieve a good match with the detector cold screen. Fig. 3 displays the ray trace of the mid-wave infrared optical system. The optical path of the system is composed of seven silicon/germanium lenses. Except for lens 2 and lens 5, which are aspherical, the rest of the lenses are spherical. Between lenses 4 and 5, and between lenses 5 and 6, plane mirrors are placed, respectively, for optical path folding. The exit pupil of the optical system is located 19.8 mm in front of the image, which satisfies the exact match with the detector's cold shield and achieves a 100% cold shield effect.

In the process of optical system imaging, there will be phase differences. After passing through the optical system, the light emitted by the object is no longer concentrated at a point on the image plane. It forms an irregular-shaped dispersion spot called a spot diagram. After the point light source passes through the optical system, diffraction images are formed on different sections of the image plane. The distribution of points in the plot can be approximately equivalent to the energy distribution of the spot. The distribution of speckle energy can reflect optical aberrations and defects very sensitively. The density of points in the spot diagram can be used to measure the imaging quality of the optical system. The shape of the spot diagram is used to roughly judge the aberrations in the system. Because of the convenient calculation and intuitive graphic image of the spot diagram, the spot diagram is commonly utilized to evaluate the image quality of the optical system. Fig. 4 depicts the spot diagrams of the mid-wave infrared optical system for multiple fields. The grid on the aperture surface is used to determine the intersection point of the uniform light passing through the optical system. The rms radius of the diffused spot in the full field of view of the optical system design is within  $3.6 \mu\text{m}$ , which is close to the diffraction limit. Thus, the optical system of the mid-wave infrared imager system can ensure the sharpness of the imaging quality.

The modulation degree is defined as the contrast ratio of the sinusoidal grating fringes. The ratio of the modulation degree of a fringe image to the actual optical system fringe image is the modulation transfer function (MTF), which represents the frequency response of the optical system to the amplitude of the sinusoidal grating fringe. When a lens achieves the output of the lens being the input of the lens, it is said to be a perfect lens.

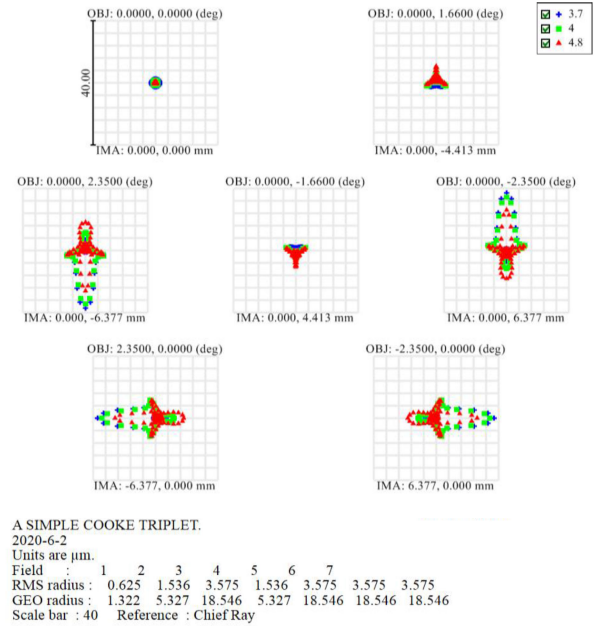


Fig. 4. Spot diagrams of the telescope for multiple fields of three wavelengths of 3.7, 4, and  $4.8 \mu\text{m}$ . Central FOV is considered as 0 FOV. The left view is positive and the right is negative.

However, because there are many factors in the design of a lens, the ideal lens is impossible. These factors are not only related to the image difference between the optical systems but also the diffraction effects of the optical system. Each component within an optical system has an associated MTF that contributes to the overall MTF of the system, including imaging lenses, camera sensors, and so on. Therefore, the final MTF of an optical system is the product of all the MTF curves of its components. The modulation degree of the image will only decrease, not increase, and the MTF of any spatial frequency is less than or equal to one. This technique of measuring the optical frequency is how many lines can be presented in the range of one millimeter. Its units are represented by line/mm. MTF was generated by ZEMAX software.

The MTF measurement experiment was carried out at a standard atmospheric pressure and a laboratory ambient temperature of 295 K. Fig. 5 demonstrates the MTF of a mid-wave infrared imager system for different FOVs at normal temperature and pressure. An MTF of 0.6 for the optical system is sufficient for imaging requirements. The MTF of the optical system in the mid-wave infrared imager system is better than  $0.6@33.33$  line/mm under different FOVs. It is proven that the optical system of the mid-wave infrared imager system has an excellent optimized design.

### C. Imaging Electronics Design

Imaging electronics mainly provides the bias voltage and timing required for the detector to work. At the same time, the video signal output by the detector is collected. After the analog-to-digital conversion of a video signal, the image data is output through the data transmission interface. Fig. 6 shows a functional block diagram of imaging electronics. The functions

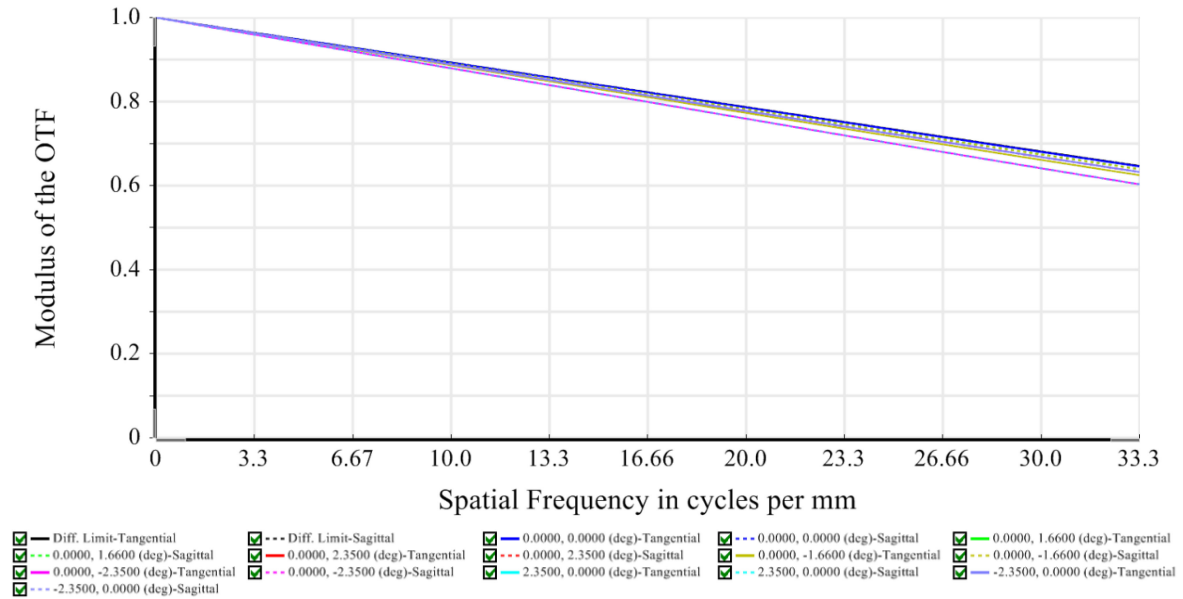


Fig. 5. MTF of mid-wave infrared imager system for different FOVs.

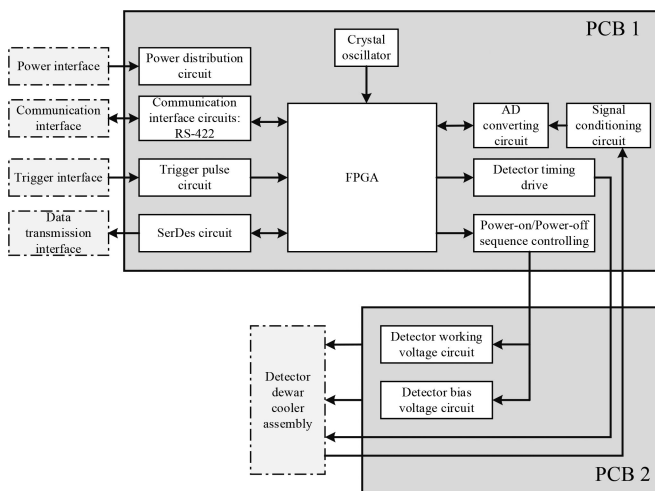


Fig. 6. Imaging Electronics Functional Block Diagram.

of imaging electronics are mainly integrated on two printed circuit boards (PCB). PCB 1 is a control board for controlling data. PCB 2 is the detector interface board to ensure the normal operation of the detector.

The control board integrates many circuit modules, including a communication interface circuit, trigger pulse circuit, high-speed image data transmission circuit, analog to digital (AD) conversion circuit, signal conditioning circuit. These circuits are linked by a large number of I/O pins in a field programmable gate array (FPGA). A logic gate unit is used to realize the digital logic function of each pin level. A crystal oscillator provides basic clock signals for the FPGA. The communication interface circuit is responsible for supporting the communication interface in transmitting the control signal. RS-422 is one of the serial data communication interface standards. Due to the support of point-to-multi bidirectional communication, it has been

selected as the communication interface standard. A trigger pulse circuit is specially used to generate control pulses that switch the circuit. It can not only produce electrical pulses but also amplify, transform, and shape electrical pulses. The high-speed image sends high-speed image data outward through the data transmission interface. The data transmission rate is approximately 6 Mbps. Serialize/Deserialize is a serial communication technology with time division multiplexing and point-to-point (P2P). It can convert multiple low-speed parallel signals into high-speed serial signals at the transmitter. Then, the high-speed serial signal is converted to a low-speed parallel signal at the receiver. This P2P serial communication technology makes full use of channel capacity to improve signal transmission speed. The AD conversion circuit realizes the digitization of the analog signal obtained. The signal conditioning circuit is the active filtering and amplitude adjustment of the video signal output by the detector to meet the input dynamic range requirements of the AD converter.

A detector working voltage circuit and a detector bias supply circuit are the main components of the detector interface board. The detector bias supply circuit is responsible for supplying high-quality bias for the detector to ensure that it is in the best working state. The detector's working voltage circuit provides the normal working timing of the detector. This part of the timing will be flexibly adjusted according to the imaging parameters provided by the control signal, like integral time, frame frequency, and readout band.

#### D. Structural Design

The structure design is an important part of the general design and one of the keys to ensuring the imaging quality of the mid-wave infrared imager. The optical system, the focal plane component form, and the structural interface play a role in its structure. The photoelectric load structural design provides a

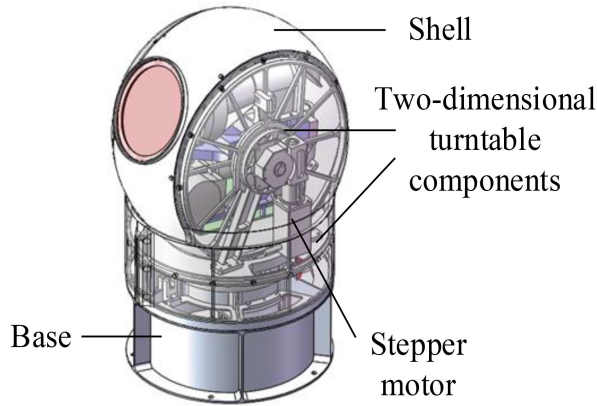


Fig. 7. Sectional view of the infrared optoelectronic system.

strong guarantee for the accuracy and precision of each imaging optical element of the camera during the life period from the assembly and inspection to use. In summary, the basic requirements for structural design are as follows.

- 1) *Excellent structural stiffness and strength.* It is ensured that the camera structure can adapt to the harsh mechanical environment, and its components do not produce trace amounts. It is necessary to ensure that the deformation of the camera structure does not cause the surface accuracy of the optical element, and the relative position change between the elements under the mechanical environment transformation does not exceed the allowable value of the optical design.
- 2) *High thermal stability.* Under the condition of large space temperature variation, the thermal distortion of the camera mirror and the supporting structure meets the tolerance requirements, particularly the matching of the linear expansion coefficient between the mirror and the supporting structure materials.
- 3) *Easy to assemble and test.* It can reduce the human and material resources needed during the assembly process as well as the complexity of subsequent adjustment.

The sectional view of the infrared optoelectronic system is shown in Fig. 7. The 2-D turntable support assembly is the main support structure of the whole infrared photoelectric system to realize the pitch and yaw movement of the system. An internal support frame is installed inside the turntable, on which all optical cameras are mounted. The internal optical component includes receiving lenses, mirrors, a mid-wave infrared detector, and its circuitry. The support base is connected to the platform body, which plays the role of cushioning and shock absorption.

The uncertainties of the stable platform include the static and dynamic uncertainties of the system. The air drive chain of the driving mechanism can cause static uncertainty in the system. The system's dynamic uncertainty is caused by the insufficient stiffness of the transmission chain, such as the elastic deformation of the transmission shaft and transmission components. The azimuth and yaw frame axes of the two-axis two-frame system are the platform's stable axes, which must achieve high stability and accuracy. For this reason, the intermediate links

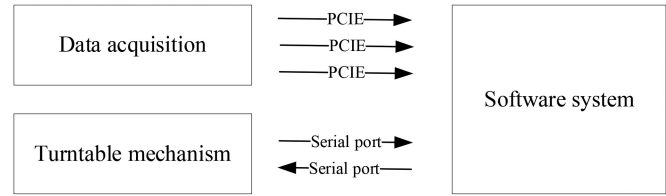


Fig. 8. Schematic diagram of the data flow in target tracking.

of the transmission chain should be simplified as much as possible to minimize the uncertainty caused by the transmission. Common gear and screw drives, including harmonic gear drives with the highest transmission accuracy, inevitably introduce uncertainty, resulting in a decrease in stability accuracy. To reduce the abovementioned uncertainty, the drive mechanism of the two-axis two-frame system needs to use a locked-rotor stepping motor with superior control performance and high output torque to achieve excellent mechanical characteristics of the drive mechanism.

The shell is made of 3D-printed plastic to reduce the weight of the machine. The internal ring rib ensures adequate rigidity and strength. The support ring frame is designed inside the infrared photoelectric system, and the material is light glass fiber reinforced plastic. The overall structure is compact and has a certain resistance to deformation.

### III. REAL-TIME TARGET DETECTION AND TRACKING

#### A. Target Tracking Method Combined With Hardware

The software system of the MWIR imager system is embedded in a single-board computer. National Instruments (NI) released the NI-9651 single-board computer. The NI-9651 is the latest technology in their line of single-board reconfigurable input/output (sbRIO) products. The NI-9651 takes the Xilinx Zynq-7020 System on Chip and pairs it with 512 MB of memory and 1 GB of nonvolatile flash. In addition, the NI-9651 runs the Linux kernel. The program development environment running on the NI-9651 is Laboratory Virtual Instrument Engineering Workbench (LABVIEW) established by NI. As a general programming system, LABVIEW has a large function library that can realize various programming tasks. To achieve real-time data processing, the algorithm must be encapsulated in library functions that can be called by LABVIEW. First, algorithm programs are compiled under the MATLAB R2015b (Win32) platform. The application compiler function in the MATLAB system has a generic COM component (GCC). The GCC can build the library compiler project and package all the script files in the project. Finally, a packaged project is generated as a dynamic link library for the PC side of LABVIEW to invoke.

Fig. 8 displays the data flow during the execution of the target tracking function. After the optical system receives the radiation signal, the data acquisition will transmit the acquired infrared image data to the software system through the three-way PCIE interface. The roll and pitch information data read from the encoder of the turntable mechanism is transmitted through the serial port to the software system to obtain the pitch and roll

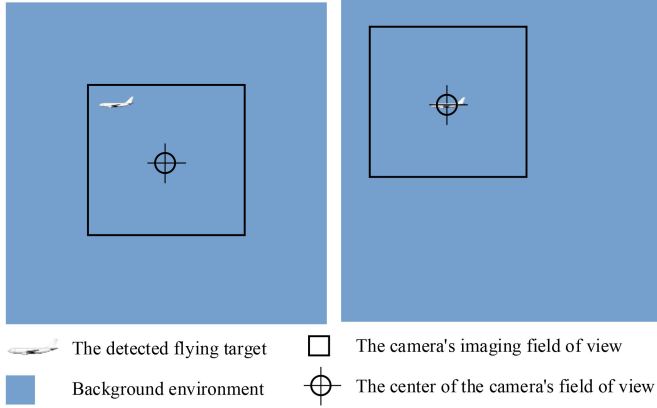


Fig. 9. Moving process of the camera field of view.

position information of the current camera imaging. When the algorithm detects a flying target with a tracking value in the infrared image data, the horizontal and vertical pixel difference between the current position of the target and the center point of the image is output. Combined with the position information during imaging, a control command is sent to the motor driver of the turntable mechanism through the serial port. The camera's field of view rotates to the centroid position of the detection target, ensuring that the target is always flying in the field of view. The continuous real-time tracking of the target can be realized. The moving process of the camera field of view is exhibited in Fig. 9.

The software systems inside the mid-wave infrared imager system run on a single-board computer. A single-board computer has limited computing resources and computing space. At the same time, the imager system has high timeliness and accuracy requirements for the output of target detection results. Therefore, the target detection algorithm must have the features of simple algorithm complexity, fast running speed, and low false alarm rate to meet the application requirements of real-time tracking.

### B. Target Detection Algorithm

The schematic diagram of traditional FAST corner detection is shown in Fig. 10 [64]. Point  $P$  is the center pixel. To determine whether point  $P$  is a corner point, it is necessary to check whether there are  $n$  consecutive pixel points in the 16 pixels on the ring around point  $P$ , whose values are all greater than or less than the value of the center pixel point  $P$ . If it exists, the center point such as point  $P$  is called a bright corner point or a dark corner point. The specific discriminant is

$$S_{x \in \Omega} = \left\{ \begin{array}{l} d, I_{x \in \Omega} \leq I_p - t \\ s, I_p - t \leq I_{x \in \Omega} \leq I_p + t \\ b, I_{x \in \Omega} \geq I_p + t \end{array} \right\} \quad (1)$$

where  $\Omega$  denotes an annular area with a radius of 3 around the center point  $P$ ,  $x$  symbolizes a pixel in  $\Omega$ ,  $S$  denotes the feature value of the pixel in  $\Omega$ ,  $I$  denotes the value of the pixel in  $\Omega$ ,  $I_p$  denotes the value of the center point  $P$ ,  $t$  denotes threshold,  $d$  represents a point darker than the center point  $P$ ,  $s$  denotes a

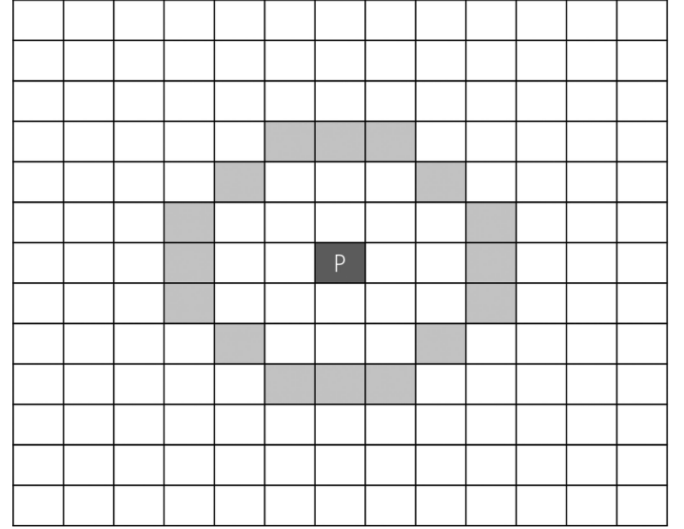


Fig. 10. Schematic diagram of traditional FAST corner detection algorithm.

point similar to the center point  $P$ , and  $b$  denotes a point brighter than the center point  $P$ . Then, based on the category of  $S$ , it is determined whether  $P$  is a corner point and the category of the corner point.

The traditional FAST method cannot be applied directly to detect small infrared target for the following reasons.

- 1) Small infrared target is easily affected by noise, and infrared image noise is unavoidable.
- 2) If there has a complex background in the infrared image, it is easy to affect FAST corner detection.
- 3) Infrared small targets approximate Gaussian spots, and there are no sharp corners for detection.

As a result, FAST was rarely used in the detection of small infrared targets. Based on the abovementioned three points and the characteristics of scatter noise and Gaussian-like small infrared targets, an IFAST target detection algorithm for small infrared targets is proposed, as illustrated in Fig. 11.

Point  $P$  is the center pixel. The dark circle around the center pixel  $P$  is the area  $\Omega_2$  (including 8 pixels), and the light circle with a radius of 3 in area  $\Omega_1$  (including 16 pixels). The criterion for judging is shown in

$$I_p^d = \left\{ \begin{array}{l} I_p - I_{\Omega_1}^9, I_p - I_{\Omega_1}^9 \geq t_1 \ \& \ |I_p - I_{\Omega_2}^8| \leq t_2 \\ 0, \text{ else} \end{array} \right\} \quad (2)$$

where  $\&$  denotes a logical relationship AND,  $t_1 = c_1 \times M$ ,  $t_2 = c_2 \times M$ ,  $t_1$  and  $t_2$  denote the threshold.  $M$  represents the maximum value of the range of values in the image pixels,  $c_1$  is the experience value, generally 0.1,  $c_2$  is the experience value, generally 0.05,  $I_p^d$  denotes the feature value of the point  $P$ ,  $I_p$  signifies the value of the point  $P$ ,  $I_{\Omega_1}^9$  denotes the value of the ninth pixel  $\Omega_1$  sorted from small to large, and  $I_{\Omega_2}^8$  denotes the largest value of the pixel in  $\Omega_2$ . The larger the value of  $I_p^d$ , the greater the possibility of point  $P$  being the target point.

Then, by comparing the normalized infrared image  $I_p^d$  with the normalized original infrared image  $I$ , the target reliable point



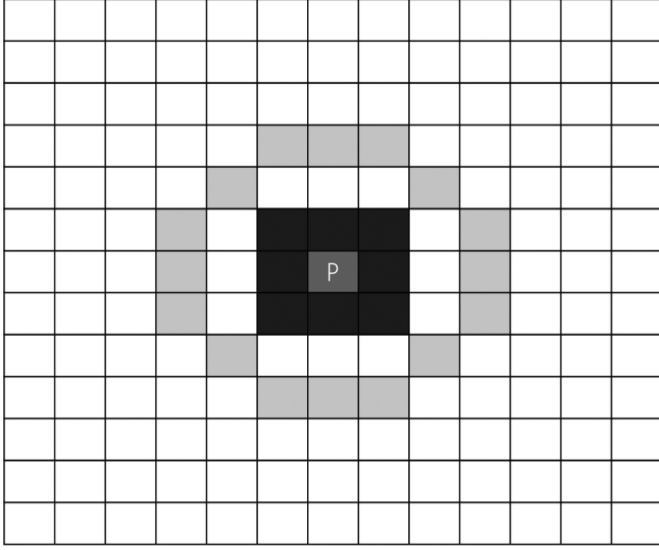


Fig. 11. Schematic diagram of infrared small target detection.

is obtained after removing possible scattering noise

$$I_{re} = \begin{cases} 1, & I_p^d / I_{p\max}^d \geq I / I_{\max} \\ 0, & I_p^d / I_{p\max}^d < I / I_{\max} \end{cases} \quad (3)$$

where  $I_{re}$  denote the target reliable point,  $I_{p\max}^d$  denotes the maximum pixel value in  $I_p^d$ , and  $I_{\max}$  denotes the maximum pixel value in  $I$ .

#### IV. EXPERIMENT

##### A. Measurement Metrics and Comparison Methods

In this article, three performance evaluation metrics, signal to clutter ratio gain (SCRG), background suppression factor (BSF), and receiver operating characteristic (ROC) curve, are selected to quantitatively evaluate the performance of small-target detection methods [65], [66].

SCRG [65] is employed to analyze the target enhancement performance of the method. The higher the SNRG, the better the enhancement effect of the target. The definitions are described as

$$\text{SCRG} = \frac{\text{SCR}_{\text{out}}}{\text{SCR}_{\text{in}}} \quad (4)$$

$$\text{SCR} = \frac{|\mu_t - \mu_b|}{\sigma_b} \quad (5)$$

where  $\mu_t$  symbolizes the mean value of the target,  $\mu_b$  denotes the mean value of the background,  $\sigma_b$  represents the standard deviation of background,  $\text{SCR}_{\text{out}}$  denotes the SCR of the processed image, and  $\text{SCR}_{\text{in}}$  denotes the SCR of the original image.

BSF [66] is used to assess the background suppression performance of the method. The higher the BSF, the better the suppression performance of the method for image background clutter. It is defined as

$$\text{BSF} = \frac{\sigma_{\text{in}}}{\sigma_{\text{out}}} \quad (6)$$

where  $\sigma_{\text{in}}$  denotes the standard deviation of the background clutter in the original infrared image and  $\sigma_{\text{out}}$  denotes the standard deviation of the background clutter in the processed image.

True positive rate (TPR) is the probability of true detection. False positive rate (FPR) is the probability of false detection. ROC curve [65] is drawn with the FPR as abscissa and the TPR as ordinate. ROC curve is a widely utilized metric to quantitatively depict the dynamic relationship between FPR and TPR. The corresponding method is better if the ROC curve is closer to the top-left corner. They are formulated as

$$\text{TPR} = \frac{\#\text{true pixels detected}}{\#\text{total true pixels}} \quad (7)$$

$$\text{FPR} = \frac{\#\text{false pixels detected}}{\#\text{total image pixels}}. \quad (8)$$

##### B. Comparison Experiment

Considering the diversity of targets and complexity of the background, six infrared datasets [67] with different background complexities and varying target pixel sizes are utilized to test the performance. The detailed information is listed in Table II. The targets have different types, spatial sizes, less texture, and detailed information. Furthermore, the background is usually complex and has serious noise/clutter. The images have low SNR values, and the contrast between targets and background is not significant. All of these factors make the targets easily submerged in the background, making small-target detection difficult.

This article compares nine infrared target detection methods; three spatial domain-based methods (ERG [28], Top-Hat [31], and Max-Mean [32]), one frequency domain-based method (WPT-HOS [38]), three contrast-based methods (LCM [39], MPCM [42], and RLCM [44]), and two low-rank matrix-based methods (NIPPS [52] and RIPT [54]). Fig. 12 displays the target images processed by the nine detection algorithms and the IFAST method proposed in this article. At the same time, 3-D stereograms of the processed images are drawn to demonstrate the processing findings more intuitively. Fig. 12 selects one representative frame from six infrared image datasets. Fig. 12(a) is the original images of datasets and the corresponding 3-D stereograms. Fig. 12(b)–(k) is the detection results of different algorithms and the corresponding 3-D stereograms.

By comparing the detection results in Fig. 12, almost every algorithm in dataset 1 can identify a single target under a simple sky background. NIPPS and MPCM only detect a part of the target, and there is a large omission. Although ERG detects the target completely, there is also an obvious the false detection. LCM also targets the false detection of isolated noise points. Max-Mean failed to achieve a clear segmentation of the target edge. Top-Hat, Max-Mean, NIPPS, and RIPT cannot suppress background clutter effectively, and there is a lot of noise in the background. WPT-HOS and IFAST have more accurate and clearer detection. In dataset 2, there is interference from the complex ground background. Since the inhomogeneity introduced by the optical system is not effectively compensated, a noise superimposition like the shape of a pot lid appears in the

TABLE II  
DETAILS OF THE TEST INFRARED DATASET

Datasets	Frame	Image Size	Target Pixels	Average SCR	Image Description
Dataset 1	398	256×256	16×10	7.403	A single target in the sky background. Stripe noise and outliers exist in the sky background. Target with changing size and shape.
Dataset 2	100	256×256	11×10	1.368	A single target in sky background. Interference from a complex background on the ground. Image is superimposed with non-uniform noise.
Dataset 3	30	320×253	10×8	2.012	A single target in the sky background. Cloudy background, many clutters. Cloud and targets overlap.
Dataset 4	30	640×520	3×8	2.350	18 small targets in the sky background. Cloudy background, many clutters. Target with changing size and shape.
Dataset 5	30	256×200	2×3	1.192	A single target in complex cloud background. Clouds and target overlap. Low target SCR.
Dataset 6	150	256×256	2×2	4.260	A small target in the ground background. Messy and complex background. Heavy noise.

image. From Fig. 12, except for ERG, MPCM, and IFAST, many methods suffer from the complex background of the ground. Whereas MPCM misses most of the target and ERG still has obvious false detection. The clouds in the sky background of dataset 3 are thick and cluttered. The detection results of Top-Hat, Max-Mean, and WPT-HOS are greatly affected by the clouds. In LCM, MPCM, and RLCM, the centroid position of the target was found while suppressing the background noise, but in doing so, these methods lost some of the target information. ERG can accurately identify all target pixels and achieve good background clutter suppression. However, ERG's extremely high accuracy comes at the expense of adding falsely detected pixels. Only IFAST eliminates the interference of cloud clutter and accurately identifies the target, while the detection results of the other techniques exist in false alarms caused by a lot of sky background.

Dataset 4 comprises 18 infrared targets. The detection results of each algorithm are compared. The ERG detects eight targets, Top-Hat detects 17 targets, Max-Mean detects 13 targets, WPT-HOS detects 0 targets, LCM detects 13 targets, MPCM detects 16 targets, RLCM only detects one target, and the NIPPS detects 19 targets, including many false alarms. Both RIPT and IFAST correctly detect all 18 targets. For a low SCR infrared target in dataset 5, WPT-HOS and LCM can no longer recognize the target, and regard the data in the image as the background. MPCM, RLCM, and RIPT have the phenomenon of misidentifying large clouds as targets. NIPPS and IFAST successfully separated of complex background and low SCR targets. In dataset 6, a small-sized target in a complex ground background greatly increases the difficulty of target detection. The target detection results for dataset 6 indicate that only IFAST has obtained significant detection results for single target detection under complex ground background. The other approaches are affected by the ground background and are incapable of detecting targets. In general, the IFAST has higher accuracy for single or multiple target detection, better stability, and robustness in

complex environments when compared to other methods. IFAST can effectively suppress the impact of the ground background on infrared target detection. It improves the feasibility of detection results and facilitates subsequent tracking and identification. From the detection results, IFAST has a stable detection effect on infrared small target images ranging from several pixels to dozens of pixels.

SCRG, BSF, and running time are the performance metrics of various algorithms. The test results of various algorithms are listed in Tables III–V. SCRG represents the target enhancement ability of the algorithm. BSF represents the background suppression ability of the algorithm. Running time represents the time it takes for the algorithm to detect a single frame of an image. In terms of the operation time, IFAST is slightly slower than Top-Hat and WPT-HOS. On the other hand, by combining SCRG and BSF, IFAST can not only suppress the influence of background clutter but also enhance the target and highlight the target position. NIPPS and RIPT are effective in suppressing background, but the computation time of NIPPS and RIPT for each frame is too long to meet the real-time requirements. Excluding the lack of advantages of MPCM in smoothing the background, MPCM still has some advantages in enhancing the contrast of the target and shortening the operation time.

Table VI lists TPR obtained through various methods of datasets. TPR represents the accuracy of the method to detect the target. Table VII lists FPR obtained through different strategies of datasets. FPR stands for the probability that the method incorrectly detects the target. According to TPR and FPR, the ROC curves of datasets are drawn and displayed in Fig. 13. The ROC curve closer to the upper left corner corresponds to the better comprehensive detection performance of the method. For the ROC curves of different datasets in Fig. 13, the ROC curve of the IFAST is more concentrated in the upper left corner than the ROC curve of other algorithms. Therefore, IFAST is considered to have the best comprehensive performance.

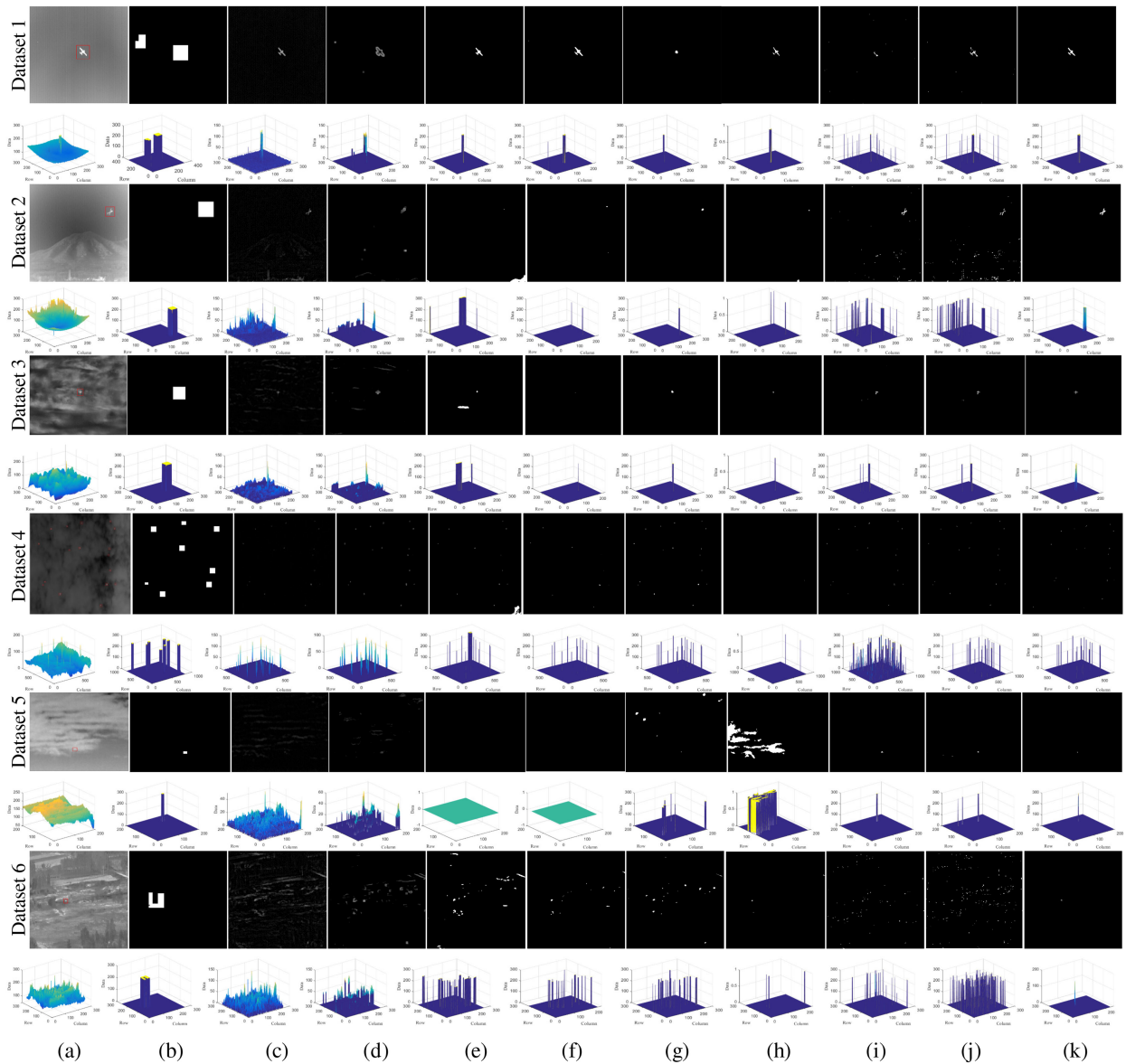


Fig. 12. Detection results of different algorithms and the corresponding 3-D stereograms. (a) Original datasets. (b) ERG. (c) Top-Hat. (d) Max-Mean. (e) WPT-HOS. (f) LCM. (g) MPCM. (h) RLCM. (i) NIPPS. (j) RIPT. (k) IFAST.

### C. Outfield Experiment

Two field imaging experiments were carried out to validate the performance of the mid-wave infrared imager system in terms of real-time target tracking. The results are reported herein.

The first field test was conducted to confirm the integrity of the compact mid-wave infrared imager system's various performance and functions. The observation site was the rooftop on the eighth floor of Building One, the Shanghai Institute of Technical Physics, the Chinese Academy of Sciences, Shanghai, China ( $121^{\circ}29'30.14\text{E}$ ,  $31^{\circ}17'8.98\text{N}$ ) on June 5, 2021. The weather was sunny and breezy during the experiment, and the temperature was approximately  $27^{\circ}\text{C}$ . The general direction of the initial alignment of the mid-wave infrared imaging system was Shanghai Hongqiao Airport, which was about 21 km away. The area over the airport where the aircraft's departure route

may pass was used as the range for the infrared imaging system to scan and image. The acquired infrared image was subjected to target detection to determine whether an aircraft target was captured during the search process. Once the aircraft target was detected, the center of the field of view of the infrared imaging system was immediately adjusted to align with the target position to ensure subsequent tracking of the target. The images captured during target detection and tracking are shown in Fig. 14. The image in Fig. 14(a) is the presence of an aircraft target detected within the imaging field of view. The images in Fig. 14(b)–(d) were captured by the infrared imaging system while adjusting the position and tracking the target according to the target detection result of the previous frame. When the target is detected in Fig. 14(a), the center position of the target is output to the infrared imaging system controller. The controller quickly adjusts the center of the field of view to the center

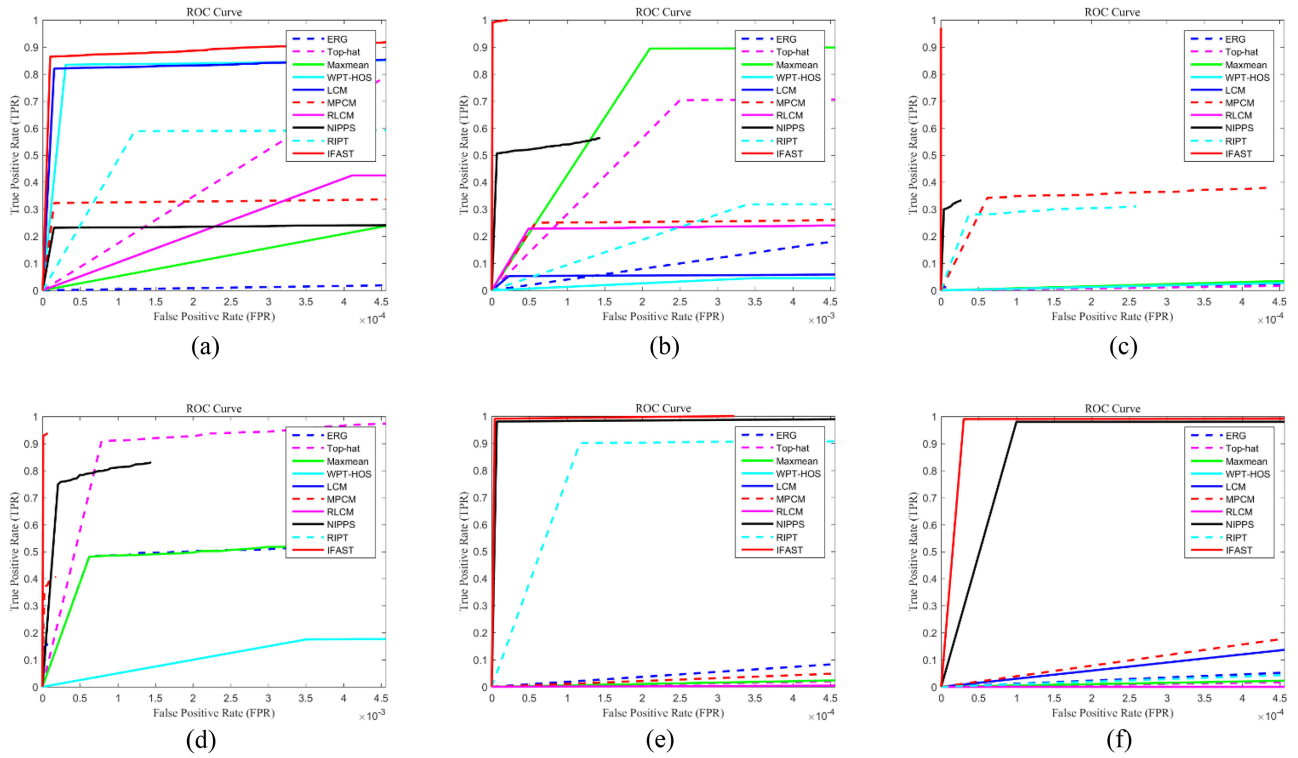


Fig. 13. ROC curves of different algorithms for different datasets. (a) Dataset 1. (b) Dataset 2. (c) Dataset 3. (d) Dataset 4. (e) Dataset 5. (f) Dataset 6.

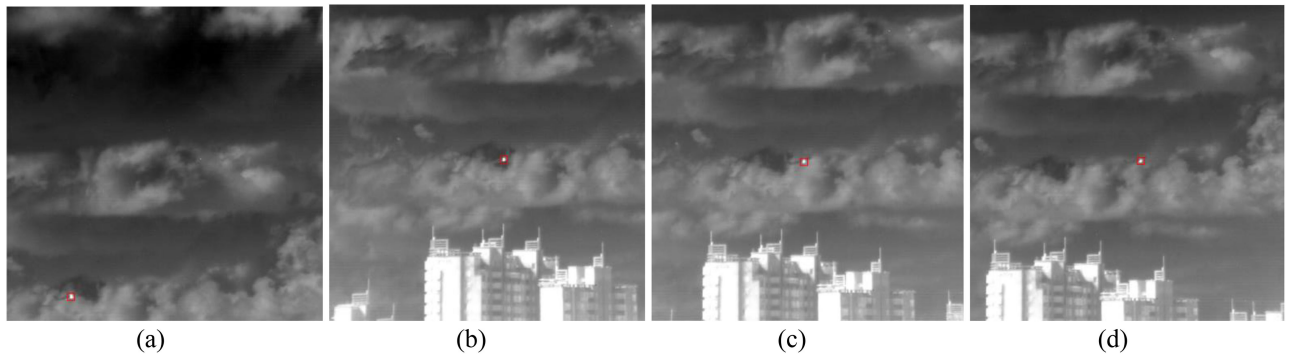


Fig. 14. Infrared target images with an approximate distance of 21 km acquired by a compact mid-wave infrared imager system during the tracking process.

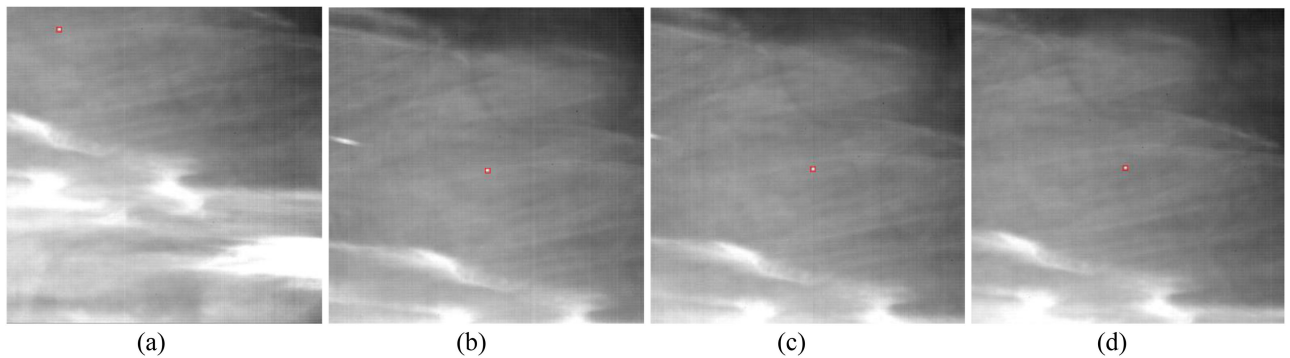


Fig. 15. Infrared target images with an approximate distance of 60 km acquired by a compact mid-wave infrared imager system during the tracking process.

TABLE III  
SCRG OBTAINED THROUGH DIFFERENT METHODS OF DATASETS

Dataset	ERG	Top-Hat	Max-Mean	WPT-HOS	LCM	MPCM	RLCM	NIPPS	RIPT	IFAST
1	6.670	10.282	8.2941	6.631	1.236	<b>23.846</b>	3.975	7.402	7.228	19.511
2	36.634	7.647	7.170	12.719	2.913	48.168	31.647	36.308	17.651	<b>314.716</b>
3	3.601	2.782	3.182	10.279	141.395	30.280	47.639	<b>755.567</b>	250.337	492.703
4	4.117	19.905	4.117	10.034	33.235	187.271	136.230	104.062	<b>Inf</b>	<b>Inf</b>
5	2.677	2.028	2.056	\	\	7.609	1.766	145.373	130.133	<b>353.034</b>
6	2.356	1.459	1.228	0.759	5.941	4.264	15.800	28.823	14.495	<b>29.676</b>

\ denotes no target detected or no data.

TABLE IV  
BSF OBTAINED THROUGH DIFFERENT METHODS OF DATASETS

Dataset	ERG	Top-Hat	Max-Mean	WPT-HOS	LCM	MPCM	RLCM	NIPPS	RIPT	IFAST
1	1.488	4.829	10.631	11.371	1.044	2.092	1.656	34.162	24.365	<b>47.887</b>
2	<b>234.020</b>	9.6551	8.048	2.289	1.076	1.845	5.652	55.385	30.776	79.637
3	174.753	6.929	5.464	2.755	28.836	2.401	9.425	<b>1723.446</b>	671.615	258.360
4	132.742	24.471	132.742	2.584	7.617	5.336	18.181	241.155	<b>Inf</b>	<b>Inf</b>
5	128.561	6.601	5.133	\	\	1.059	0.379	370.088	410.567	<b>4496.824</b>
6	<b>200.612</b>	2.814	2.184	1.229	2.320	1.028	5.733	43.896	24.750	94.248

TABLE V  
RUNNING TIME OF EACH DETECTION METHOD OF DATASETS

Dataset	ERG	Top-Hat	Max-Mean	WPT-HOS	LCM	MPCM	RLCM	NIPPS	RIPT	IFAST
1	0.191 s	0.0163 s	0.728 s	0.061 s	17.915 s	0.106 s	2.782 s	4.632 s	1.303 s	0.101 s
2	0.189 s	0.0164 s	0.704 s	0.059 s	17.928 s	0.108 s	2.780 s	4.517 s	1.062 s	0.096 s
3	0.239 s	0.0187 s	0.905 s	0.0642 s	22.552 s	0.163 s	5.001 s	6.956 s	1.509 s	0.172 s
4	1.940 s	0.876 s	5.835 s	0.339 s	161.702 s	0.724 s	12.470 s	5.101 s	11.194 s	0.579 s
5	0.132 s	0.0153 s	0.564 s	0.0495 s	13.837 s	0.0843 s	1.510 s	2.152 s	0.640 s	0.0728 s
6	0.188 s	0.0157 s	0.889 s	0.0546 s	18.032 s	0.302 s	2.831 s	4.179 s	2.276 s	0.0844 s

TABLE VI  
TPR OBTAINED THROUGH DIFFERENT METHOD OF DATASETS

Dataset	ERG	Top-Hat	Max-Mean	WPT-HOS	LCM	MPCM	RLCM	NIPPS	RIPT	IFAST
1	0.994	1	0.892	0.907	0.901	0.259	0.247	0.157	0.536	0.960
2	1	0.782	0.992	0.0504	0.0588	0.277	0.253	0.563	0.353	1
3	1	0.736	0.966	0.195	0.0115	0.379	0.092	0.333	0.310	0.971
4	0.534	1	0.534	0.194	0.159	0.406	0.011	0.830	0.259	0.937
5	1	1	1	\	\	0.333	0.500	1	1	1
6	0.500	1	1	0	0.500	1	0	1	0.500	1

of the target mass from Fig. 14(a), and continues to image to obtain Fig. 14(b). Then, according to the target center position output in Fig. 14(b), adjust the imaging center field of view of the controller, followed by imaging to obtain Fig. 14(c). Based on the adjusted camera field of view in Fig. 14(c), Fig. 14(d) is captured. From Fig. 14(b)–(d), the deviation of the target from the center of the field of view is small after adjusting the field of view of the infrared imaging system. It is verified that the target detection algorithm and the target tracking hardware implementation have excellent real-time performance and can meet the needs of real-time target tracking.

A remote-sensing experiment was carried out on Oct 25, 2021, to verify the ability of a compact mid-wave infrared imager system to obtain infrared data and track the infrared target at

a further distance. The observation site was at the top of Mount Tai, Taian City, Shandong Province, China (117° 06' 13.96E, 36° 15' 24.59' N). The Beijing–Guangzhou route has always been the busiest in China, with numerous daily flights frequenting between Guangzhou Baiyun Airport and Beijing Capital Airport. The altitude of the test site was about 1500 m, and the shortest straight-line distance from Mount Tai to this route was about 60 km. Therefore, the Beijing–Guangzhou route was selected as the area for long-distance observation experiments due to its abundant aerial target samples. The images acquired by the mid-wave infrared imager system during the detecting tracking process are shown in Fig. 15. Imaging at long distances reduces the size of the target significantly. In the face of cluttered and scattered cloud backgrounds, IFAST can still maintain high

TABLE VII  
FPR OBTAINED THROUGH DIFFERENT METHOD OF DATASETS

Dataset	ERG	Top-Hat	Max-Mean	WPT-HOS	LCM	MPCM	RLCM	NIPPS	RIPT	IFAST
1	0.0219	5.188e-4	0.0016	3.052e-5	1.526e-5	1.525e-5	4.112e-4	1.488e-5	1.221e-4	1.064e-5
2	0.0226	0.0025	0.0021	0.0035	2.289e-4	5.798e-4	4.883e-4	6.859e-5	0.0034	0
3	0.0187	0.0184	0.0114	0.0029	0	6.176e-5	0	3.896e-6	3.706e-5	0
4	6.229e-4	7.859e-4	6.229e-4	0.0035	0	2.595e-5	1.854e-6	2.066e-4	0	0
5	0.0049	0.0208	0.0173	\	\	0.0028	0.0486	6.818e-6	1.172e-4	3.103e-6
6	0.0039	0.0242	0.0181	0.0069	0.0015	0.0023	1.984e-4	1.000e-4	0.0047	1.472e-5

\ denotes no target detected or no data.

accuracy and stability. In Fig. 15(a), IFAST detected the infrared target and immediately output the target center position to the infrared imager system controller. After adjusting the center field of view of the infrared imager system to overlap with the center position of the target in Fig. 15(a), Fig. 15(b) is obtained by imaging. Subsequently, the infrared imager system sequentially acquired images of Fig. 15(c) and (d).

Both field tests can achieve clear imaging of long-distance small target, confirming the accuracy of the target detection algorithm for small target detection and the stability of real-time target tracking.

## V. CONCLUSION

Considering the development trend of compact and lightweight infrared photoelectric systems, a compact mid-wave infrared imaging system is developed in this article. The choice of telephoto lens and catadioptric optical design improves the compactness of the structure and enables long-distance imaging. The small imaging field of view brought about by the small optical aperture is compensated for by the large-scale rotation of the 2-D console in the yaw and pitch directions. In addition, inspired by the FAST corner detection algorithm, combined with the characteristics of small infrared targets and the characteristics of noise, an IFAST method for edge detection of small infrared target is proposed. The high real-time performance of the target detection algorithm and the advantages of the 2-D turntable provide a new strategy for real-time target tracking. After the test of the public dataset, it is proven that IFAST has a strong anti-interference ability against the complex sky and ground background in the infrared image. IFAST has good detection performance for small targets ranging from a few pixels to dozens of pixels, and has obvious advantages in reducing the false alarm rate. Both outfield tests can effectively achieve clear imaging of small targets at distances of 20 km and 60 km, and subsequent stable target tracking. The accuracy of the target detection algorithm for small target detection and the stability of real-time target tracking are thoroughly verified.

In addition, despite the accuracy of the IFAST algorithm is high, the strategy for tracking after single-frame detection lacks compensation measures for false alarm targets. In the future, we will generalize the proposed IFAST algorithm from single-frame detection to multiframe detection and consider parallel processing to improve efficiency, so as to ensure the real-time performance of subsequent target tracking.

## ACKNOWLEDGMENT

The authors would like to thank the responsible editor for his conscientiousness and hard work and also like to sincerely thank the reviewers for their comments and suggestions.

## REFERENCES

- [1] Y. Wang, L. Zhu, and Z. Yu, "Foreground detection for infrared videos with multiscale 3-D fully convolutional network," *IEEE Geosci. Remote Sens. Lett.*, vol. 16, no. 5, pp. 712–716, May 2019, doi: [10.1109/LGRS.2018.2881053](https://doi.org/10.1109/LGRS.2018.2881053).
- [2] M. Zhao, L. Li, W. Li, R. Tao, L. Li, and W. Zhang, "Infrared small-target detection based on multiple morphological profiles," *IEEE Trans. Geosci. Remote Sens.*, vol. 59, no. 7, pp. 6077–6091, Jul. 2021, doi: [10.1109/TGRS.2020.3022863](https://doi.org/10.1109/TGRS.2020.3022863).
- [3] L. Dong, B. Wang, M. Zhao, and W. Xu, "Robust infrared maritime target detection based on visual attention and spatiotemporal filtering," *IEEE Trans. Geosci. Remote Sens.*, vol. 55, no. 5, pp. 3037–3050, May 2017, doi: [10.1109/TGRS.2017.2660879](https://doi.org/10.1109/TGRS.2017.2660879).
- [4] N. Wang, B. Li, X. Wei, Y. Wang, and H. Yan, "Ship detection in spaceborne infrared image based on lightweight CNN and multisource feature cascade decision," *IEEE Trans. Geosci. Remote Sens.*, vol. 59, no. 5, pp. 4324–4339, May 2021, doi: [10.1109/TGRS.2020.3008993](https://doi.org/10.1109/TGRS.2020.3008993).
- [5] J. Jia et al., "Tradeoffs in the spatial and spectral resolution of airborne hyperspectral imaging systems: A crop identification case study," *IEEE Trans. Geosci. Remote Sens.*, vol. 60, 2022, Art. no. 5510918, doi: [10.1109/TGRS.2021.3096999](https://doi.org/10.1109/TGRS.2021.3096999).
- [6] *Handbook of Geophysics and the Space Environment*, 4th ed. Springfield, IL, USA: Air Force Syst. Command, U.S. Dept. Commerce Nat. Tech. Inf. Service, 1985.
- [7] J. Jia, Y. Wang, J. Chen, R. Guo, R. Shu, and J. Wang, "Status and application of advanced airborne hyperspectral imaging technology: A review," *Infrared Phys. Technol.*, vol. 104, 2020, Art. no. 103115, doi: [10.1016/j.infrared.2019.103115](https://doi.org/10.1016/j.infrared.2019.103115).
- [8] I. V. Znamensky and A. A. Tikhomirov, "Calculation of the attenuation of the transmission of an IR radiation flux on the inclined route in the atmosphere, taking into account the sphericity of the earth's surface," *Atmos. Ocean Opt.*, vol. 4, pp. 315–320, 2020, doi: [10.15372/AOO20200411](https://doi.org/10.15372/AOO20200411).
- [9] X. Deng, Y. M. Wang, G. C. Han, and T. R. Xue, "Research on a measurement method for middle-infrared radiation characteristics of aircraft," *Machines*, vol. 10, no. 1, Jan. 2022, Art. no. 44, doi: [10.3390/machines10010044](https://doi.org/10.3390/machines10010044).
- [10] F. Maire and S. Lefebvre, "Detecting aircraft in low-resolution multispectral images: Specification of relevant IR wavelength bands," *IEEE J. Sel. Topics Appl. Earth Observ. Remote Sens.*, vol. 8, no. 9, pp. 4509–4523, Sep. 2015, doi: [10.1109/JSTARS.2015.2457514](https://doi.org/10.1109/JSTARS.2015.2457514).
- [11] D. Cormack, I. Schlangen, J. R. Hopgood, and D. E. Clark, "Joint registration and fusion of an infrared camera and scanning radar in a maritime context," *IEEE Trans. Aerosp. Electron. Syst.*, vol. 56, no. 2, pp. 1357–1369, Apr. 2020, doi: [10.1109/TAES.2019.2929974](https://doi.org/10.1109/TAES.2019.2929974).
- [12] J. Jia et al., "Destriping algorithms based on statistics and spatial filtering for Visible-to-Thermal infrared pushbroom hyperspectral imagery," *IEEE Trans. Geosci. Remote Sens.*, vol. 57, no. 6, pp. 4077–4091, Jun. 2019, doi: [10.1109/TGRS.2018.2889731](https://doi.org/10.1109/TGRS.2018.2889731).
- [13] D. Beach, "Ultra-high-speed wide-angle catadioptric corrector system for medium-scale spherical mirror telescopes," *Opt. Eng.*, vol. 42, no. 2, pp. 405–415, 2003, doi: [10.1117/1.1534596](https://doi.org/10.1117/1.1534596).

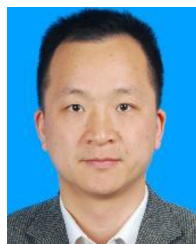
- [14] S. M. Hong, H. S. Kim, and W. K. Yu, "High performance long-wave infrared sensor with large zoom optics and high-definition television format," *Opt. Eng.*, vol. 7121, no. 2, pp. 1223–1228, 2006, doi: [10.1117/1.2403842](https://doi.org/10.1117/1.2403842).
- [15] M. C. Sanson and J. Cornell, "MWIR continuous zoom with large zoom range," *Proc. SPIE*, vol. 7760, no. 1, 2010, Art. no. 12, doi: [10.5768/jao201940.0101006](https://doi.org/10.5768/jao201940.0101006).
- [16] M. Magnusson, F. Jes, and H. Olsson, "Aerial photo-interpretation using Z/I DMC images for estimation of forest variables," *Scand. J. Forest Res.*, vol. 22, no. 3, pp. 254–266, 2007, doi: [10.1080/02827580701262964](https://doi.org/10.1080/02827580701262964).
- [17] M. Pechatnikov and Y. Raizman, "Vision map A3 system introduction and technical characteristics," *Geography*, vol. 3, pp. 55–57, 2008, doi: [10.5040/9780755620791.0005](https://doi.org/10.5040/9780755620791.0005).
- [18] H. X. He and J. S. Zhao, "An axis-zoom four fields of view MWIR optical system," *J. Infrared, Millimeter, Terahertz Waves*, vol. 36, no. 3, pp. 316–320, 2017, doi: [10.1117/12.2273177.5597173719001](https://doi.org/10.1117/12.2273177.5597173719001).
- [19] F. Zhang, C. Li, and L. Shi, "Detecting and tracking dim moving point target in IR image sequence," *Infrared Phys. Technol.*, vol. 46, pp. 323–328, 2005, doi: [10.1016/j.infrared.2004.06.001](https://doi.org/10.1016/j.infrared.2004.06.001).
- [20] M. Wan et al., "Infrared small moving target detection via saliency histogram and geometrical invariability," *Appl. Sci.*, vol. 7, 2017, Art. no. 569, doi: [10.3390/app7060569](https://doi.org/10.3390/app7060569).
- [21] S. Kim and J. Lee, "Scale invariant small target detection by optimizing Signal-to-Clutter ratio in heterogeneous background for infrared search and track," *Pattern Recognit.*, vol. 45, pp. 393–406, 2012, doi: [10.1016/j.patcog.2011.06.009](https://doi.org/10.1016/j.patcog.2011.06.009).
- [22] Q. Shu, H. Lai, L. Wang, and Z. Jia, "Multi-Feature fusion target re-location tracking based on correlation filters," *IEEE Access*, vol. 9, pp. 28954–28964, 2021, doi: [10.1109/ACCESS.2021.3059642](https://doi.org/10.1109/ACCESS.2021.3059642).
- [23] M. Zhao, W. Li, L. Li, J. Hu, P. Ma, and R. Tao, "Single-Frame infrared small-target detection: A survey," *IEEE Trans. Geosci. Remote Sens.*, vol. 10, no. 2, pp. 87–119, Jun. 2022, doi: [10.1109/MGRS.2022.3145502](https://doi.org/10.1109/MGRS.2022.3145502).
- [24] Q. Ma, X. Sun, Y. Zhang, and Y. Jiang, "Detection and recognition method of Low-altitude UAV based on infrared images," *J. Projectiles, Rockets, Missiles Guid.*, vol. 40, no. 3, pp. 150–154, 2020, doi: [10.15892/j.cnki.djzdx.2020.03.034](https://doi.org/10.15892/j.cnki.djzdx.2020.03.034).
- [25] M. Wan, G. Gu, W. Qian, K. Ren, Q. Chen, and X. Maldague, "Infrared image enhancement using adaptive histogram partition and brightness correction," *Remote Sens.*, vol. 10, 2018, Art. no. 682, doi: [10.3390/rs10050682](https://doi.org/10.3390/rs10050682).
- [26] M. Wan et al., "Total variation regularization term-based low-rank and sparse matrix representation model for infrared moving target tracking," *Remote Sens.*, vol. 10, 2018, Art. no. 510, doi: [10.3390/rs10040510](https://doi.org/10.3390/rs10040510).
- [27] M. Wan, G. Gu, W. Qian, K. Ren, and Q. Chen, "Hybrid active contour model based on edge gradients and regional multi-features for infrared image segmentation," *Opt. Int. J. Light Electron.*, vol. 140, pp. 833–842, 2017, doi: [10.1016/j.ijleo.2018.06.141](https://doi.org/10.1016/j.ijleo.2018.06.141).
- [28] C. Lou, Y. Zhang, and J. Yin, "Small target detection method based on robinson-guard filter and pixel convergence," *Acta Optica Sinica*, vol. 40, no. 15, pp. 19–28, 2020, doi: [10.3788/aos202040.1504001](https://doi.org/10.3788/aos202040.1504001).
- [29] M. M. Hadhoud and D. W. Thomas, "The two-dimensional adaptive LMS (TDLMS) algorithm," *IEEE Trans. Circuits Syst.*, vol. 35, no. 5, pp. 485–494, May 1988, doi: [10.1109/31.1775](https://doi.org/10.1109/31.1775).
- [30] Z. Q. Guan, Q. Chen, and W. X. Qian, "An adaptive background adjusting algorithm for dim target detection," *Acta Optica Sinica*, vol. 27, no. 12, pp. 2163–2168, 2007, doi: [10.1109/icnc.2010.5583371](https://doi.org/10.1109/icnc.2010.5583371).
- [31] V. T. Tom, T. Peli, M. Leung, and J. E. Bondaryk, "Morphology-Based algorithm for point target detection in infrared backgrounds," *Proc. SPIE*, vol. 1954, pp. 2–11, Oct. 1993, doi: [10.1117/12.157758](https://doi.org/10.1117/12.157758).
- [32] S. D. Deshpande, M. H. Er, R. Venkateswarlu, and P. Chan, "Max-Mean and max-median filters for detection of small targets," in *Proc. Signal Data Process. Small Targets*, 1999, pp. 74–83, doi: [10.1117/12.364049](https://doi.org/10.1117/12.364049).
- [33] C. Tomasi and R. Manduchi, "Bilateral filtering for gray and color images," in *Proc. 6th Int. Conf. Comput. Vis.*, 1998, pp. 839–846, doi: [10.1109/iccv.1998.710815](https://doi.org/10.1109/iccv.1998.710815).
- [34] D. Comaniciu, "An algorithm for data-driven bandwidth selection," *IEEE Trans. Pattern Anal. Mach. Intell.*, vol. 25, no. 2, pp. 281–288, Feb. 2003, doi: [10.1109/TPAMI.2003.1177159](https://doi.org/10.1109/TPAMI.2003.1177159).
- [35] L. Yang, J. Yang, and K. Yang, "Adaptive detection for infrared small target under sea-sky complex background," *Electron. Lett.*, vol. 40, no. pp. 1083–1085, 2004, doi: [10.1049/el:20045204](https://doi.org/10.1049/el:20045204).
- [36] G. Boccignone, A. Chianese, and A. Picariello, "Small target detection using wavelets," in *Proc. Int. Conf. Pattern Recognit.*, 1998, pp. 1776–1778, doi: [10.1109/icpr.1998.712072](https://doi.org/10.1109/icpr.1998.712072).
- [37] X. Luo and X. Wu, "A novel fusion detection algorithm for infrared small targets," in *Proc. 3rd Int. Symp. Intell. Inf. Technol. Secur. Inform.*, 2009, pp. 427–430, doi: [10.1109/IITA.2009.461](https://doi.org/10.1109/IITA.2009.461).
- [38] X. Wang and Z. Tang, "Combining wavelet packet with higher-order statistics for small IR targets detection," *Infrared Laser Eng.*, vol. 38, no. 5, pp. 915–920, 2009, doi: [10.1117/12.539886](https://doi.org/10.1117/12.539886).
- [39] C. L. P. Chen, H. Li, Y. Wei, T. Xia, and Y. Y. Tang, "A local contrast method for small infrared target detection," *IEEE Trans. Geosci. Remote Sens.*, vol. 52, no. 1, pp. 574–581, Jan. 2014, doi: [10.1109/TGRS.2013.2242477](https://doi.org/10.1109/TGRS.2013.2242477).
- [40] J. Han, Y. Ma, B. Zhou, F. Fan, K. Liang, and Y. Fang, "A robust infrared small target detection algorithm based on human visual system," *IEEE Geosci. Remote Sens. Lett.*, vol. 11, no. 12, pp. 2168–2172, Dec. 2014, doi: [10.1109/LGRS.2014.2323236](https://doi.org/10.1109/LGRS.2014.2323236).
- [41] Y. Chen and Y. Xin, "An efficient infrared small target detection method based on visual contrast mechanism," *IEEE Geosci. Remote Sens. Lett.*, vol. 13, no. 7, pp. 962–966, Jul. 2016, doi: [10.1109/LGRS.2016.2556218](https://doi.org/10.1109/LGRS.2016.2556218).
- [42] Y. T. Wei et al., "Multiscale patch-based contrast measure for small infrared target detection," *Pattern Recognit.*, vol. 58, pp. 216–226, 2016, doi: [10.1016/j.patcog.2016.04.002](https://doi.org/10.1016/j.patcog.2016.04.002).
- [43] Y. Qin and B. Li, "Effective infrared small target detection utilizing a novel local contrast method," *IEEE Geosci. Remote Sens. Lett.*, vol. 13, no. 12, pp. 1890–1894, Dec. 2016, doi: [10.1109/LGRS.2016.2616416](https://doi.org/10.1109/LGRS.2016.2616416).
- [44] J. H. Han, K. Liang, and B. Zhou, "Infrared small target detection utilizing the multiscale relative local contrast measure," *IEEE Geosci. Remote Sens. Lett.*, vol. 15, no. 4, pp. 612–616, Apr. 2018, doi: [10.1109/LGRS.2018.2790909](https://doi.org/10.1109/LGRS.2018.2790909).
- [45] J. Liu, H. Wang, L. Lei, and J. He, "Infrared small target detection utilizing halo structure prior-based local contrast measure," *IEEE Geosci. Remote Sens. Lett.*, vol. 19, 2022, Art. no. 6508205, doi: [10.1109/LGRS.2022.3162390](https://doi.org/10.1109/LGRS.2022.3162390).
- [46] J. Liu, Z. He, Z. Chen, and L. Shao, "Tiny and dim infrared target detection based on weighted local contrast," *IEEE Geosci. Remote Sens. Lett.*, vol. 15, no. 11, pp. 1780–1784, Nov. 2018, doi: [10.1109/LGRS.2018.2856762](https://doi.org/10.1109/LGRS.2018.2856762).
- [47] J. Han et al., "Infrared small target detection based on the weighted strengthened local contrast measure," *IEEE Geosci. Remote Sens. Lett.*, vol. 18, no. 9, pp. 1670–1674, Sep. 2021, doi: [10.1109/LGRS.2020.3004978](https://doi.org/10.1109/LGRS.2020.3004978).
- [48] H. Deng, X. Sun, M. Liu, C. Ye, and X. Zhou, "Small infrared target detection based on weighted local difference measure," *IEEE Trans. Geosci. Remote Sens.*, vol. 54, no. 7, pp. 4204–4214, Jul. 2016, doi: [10.1109/TGRS.2016.2538295](https://doi.org/10.1109/TGRS.2016.2538295).
- [49] P. Du and A. Hamdulla, "Infrared small target detection using homogeneity-weighted local contrast measure," *IEEE Geosci. Remote Sens. Lett.*, vol. 17, no. 3, pp. 514–518, Mar. 2020, doi: [10.1109/LGRS.2019.2922347](https://doi.org/10.1109/LGRS.2019.2922347).
- [50] Y. Chen, N. M. Nasrabadi, and T. D. Tran, "Sparse representation for target detection in hyperspectral imagery," *IEEE J. Sel. Topics Signal Process.*, vol. 5, no. 3, pp. 629–640, Jun. 2011, doi: [10.1109/JSTSP.2011.2113170](https://doi.org/10.1109/JSTSP.2011.2113170).
- [51] C. Gao, D. Meng, Y. Yang, Y. Wang, X. Zhou, and A. G. Hauptmann, "Infrared patch-image model for small target detection in a single image," *IEEE Trans. Image Process.*, vol. 22, no. 12, pp. 4996–5009, Dec. 2013, doi: [10.1109/TIP.2013.2281420](https://doi.org/10.1109/TIP.2013.2281420).
- [52] Y. Dai, Y. Wu, Y. Song, and J. Guo, "Non-Negative infrared patch-image model: Robust target-background separation via partial sum minimization of singular values," *Infrared Phys. Technol.*, vol. 81, pp. 182–194, 2017, doi: [10.1016/j.infrared.2017.01.009](https://doi.org/10.1016/j.infrared.2017.01.009).
- [53] P. Yang, L. Dong, and W. Xu, "Infrared small maritime target detection based on integrated target saliency measure," *IEEE J. Sel. Topics Appl. Earth Observ. Remote Sens.*, vol. 99, pp. 2369–2386, Jan. 2021, doi: [10.1109/JSTARS.2021.3049847](https://doi.org/10.1109/JSTARS.2021.3049847).
- [54] Y. Dai and Y. Wu, "Reweighted infrared patch-tensor model with both non-local and local priors for single-frame small target detection," *IEEE J. Sel. Topics Appl. Earth Observ. Remote Sens.*, vol. 10, no. 8, pp. 3752–3767, Aug. 2017, doi: [10.1109/JSTARS.2017.2700023](https://doi.org/10.1109/JSTARS.2017.2700023).
- [55] W. Xue, J. Qi, G. Shao, Z. Xiao, Y. Zhang, and P. Zhong, "Low-Rank approximation and multiple sparse constraint modeling for infrared low-flying fixed-wing UAV detection," *IEEE J. Sel. Topics Appl. Earth Observ. Remote Sens.*, vol. 14, pp. 4150–4166, Mar. 2021, doi: [10.1109/JSTARS.2021.3069032](https://doi.org/10.1109/JSTARS.2021.3069032).
- [56] A. A. Mills and P. J. Turvey, "1979 Newton's telescope, an examination of the reflecting telescope attributed to sir isaac newton in the possession of the royal society," *Notes Records Roy. Soc. London*, vol. 33, pp. 133–155, 1979, doi: [10.1098/rsmr.1979.0009](https://doi.org/10.1098/rsmr.1979.0009).
- [57] R. Blakley, "Cesarian telescope optical system," *Opt. Eng.*, vol. 35, no. 11, pp. 3338–3341, 1996, doi: [10.1117/1.601075](https://doi.org/10.1117/1.601075).
- [58] M. Bahrami and A. Goncharov, "Fast and compact wide-field gregorian telescope," *Proc. SPIE*, vol. 8444, 2012, Art. no. 84446H, doi: [10.1117/12.925437](https://doi.org/10.1117/12.925437).

- [59] P. Rhodes and D. Shealy, "Refractive optical systems for irradiance redistribution of collimated radiation: Their design and analysis," *Appl. Opt.*, vol. 19, pp. 3545–3553, 1980, doi: [10.1364/AO.19.003545](https://doi.org/10.1364/AO.19.003545).
- [60] J. Hoffnagle and C. Jefferson, "Design and performance of a refractive optical system that converts a gaussian to a flattop beam," *Appl. Opt.*, vol. 39, pp. 5488–5499, 2000, doi: [10.1364/AO.39.005488](https://doi.org/10.1364/AO.39.005488).
- [61] *The Design Manufacture and Test of the Aspherical Optical Surfaces*. Taipei City, Taiwan: Soochow Univ. Press, 2004.
- [62] Y. Kang, W. Liu, and R. Feng, "A refract-reflect telescope with meniscus corrector," *Opt. Precis. Eng.*, vol. 16, no. 2, pp. 215–220, 2008.
- [63] Y. Kang, W. Liu, and R. Feng, "A refract-reflect telescope with cooke as compensated lens," *Opt. Precis. Eng.*, vol. 15, no. 3, pp. 303–307, 2007.
- [64] E. Rosten and T. Drummond, "Machine learning for high-speed corner detection," in *Proc. Eur. Conf. Comput. Vis.*, 2006, pp. 430–443, doi: [10.1007/11744023\\_34](https://doi.org/10.1007/11744023_34).
- [65] H. Cui, L. Li, X. Liu, X. Su, and F. Chen, "Infrared small target detection based on weighted three-layer window local contrast," *IEEE Geosci. Remote Sens. Lett.*, vol. 19, 2022, Art. no. 7505705, doi: [10.1109/LGRS.2021.3133649](https://doi.org/10.1109/LGRS.2021.3133649).
- [66] M. Zhao, W. Li, L. Li, P. Ma, Z. Cai, and R. Tao, "Three-Order tensor creation and Tucker decomposition for infrared small-target detection," *IEEE Trans. Geosci. Remote Sens.*, vol. 60, 2022, Art. no. 5000216, doi: [10.1109/TGRS.2021.3057696](https://doi.org/10.1109/TGRS.2021.3057696).
- [67] B. W. Hui, Y. Z. Song, and H. Q. Fan, "A dataset for infrared detection and tracking of dim-small aircraft targets under ground/Air background," *Sci. Data Bank*, vol. 5, no. 3, pp. 1–12, Jan. 2020, doi: [10.11922/cs-data.2019.0074.zh](https://doi.org/10.11922/cs-data.2019.0074.zh).



**Xuan Deng** was born in China, in 1996. She received the B.E. degree in communication engineering from Ocean University of China, Qingdao, China, in 2018. She is currently working toward the Ph.D. degree in electronic science and technology with the Key Laboratory of Space Active Opto-Electronics Technology, Shanghai Institute of Technical Physics, Chinese Academy of Sciences, Shanghai, China and also with the University of Chinese Academy of Sciences, Beijing, China.

Her research interests include mid-wave infrared radiation characterization analysis, infrared data preprocessing, infrared small target detecting, and real-time tracking in remote sensing imagery.



**Yueming Wang** was born in China, in 1978. He received the B.S. degree in precision mechanical engineering from Tsinghua University, Beijing, China, in 2000, and the Ph.D. degree in electronic science and technology from the Shanghai Institute of Technical Physics, Chinese Academy of Sciences, Shanghai, China, in 2005.

He is currently a Researcher with the Shanghai Institute of Technical Physics, Chinese Academy of Sciences, Shanghai, China, also with University of Chinese Academy of Sciences, Beijing, China. His current research interests include new hyperspectral fine spectroscopic technology, hyperspectral imaging system technology in aerospace, hyperspectral calibration and data preprocessing, and high-sensitivity infrared information acquisition technology.



**Daogang He** was born in China, in 1976. He received the B.E. degree in electronic information science and technology from Shan Dong University, Jinan, China, in 1998.

He is a Senior Engineer with the Shanghai Institute of Technical Physics, Chinese Academy of Sciences, Shanghai, China, also with University of Chinese Academy of Sciences, Beijing, China. He has responsibility for research and development of high-performance imaging spectrometers. His major research interests include the electronics system design and simulation of infrared and hyperspectral imaging system.



**Guicheng Han** was born in China, in 1986. He received the B.E. degree in electronic information science and technology from Fudan University, Shanghai, China, in 2008, and the master's degree in circuits and systems from Fudan University, Shanghai, China, in 2011.

He is a Senior Engineer with the Shanghai Institute of Technical Physics, Chinese Academy of Sciences, Shanghai, China, also with the University of Chinese Academy of Sciences, Beijing, China. He has responsibility for research and development of high-performance imaging spectrometers. His major research interest includes the aerial remote sensing control system design.



**Tianru Xue** was born in China, in 1995. She received the B.E. degree in electronic information science and technology from Lanzhou University, Lanzhou, China, in 2017. She is currently working toward the Ph.D. degree in electronic science and technology with the University of Chinese Academy of Sciences, Beijing, China.

Her research interests include hyperspectral image analysis, dimension reduction, and real-time processing in remote sensing imagery.



**Yifan Hao** was born in China, in 1995. He received the B.S. degree in applied physics from Dalian University of Technology, Dalian, China, in 2018. He is currently working toward the Ph.D. degree in physical electronics with the University of Chinese Academy of Sciences, Beijing, China.

His research interests include infrared and visible light fusion and multifocus fusion of objects based on deep learning methods and classic methods.



**Xiaoqiong Zhuang** was born in China. She received the B.S. and M.S. degrees in information engineering from Nanjing Normal University, Nanjing, China, in 2004 and 2007, respectively.

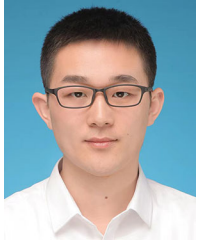
She is currently an Electronic Engineer with the Shanghai Institute of Technical Physics, Chinese Academy of Sciences, Beijing, China. Her research interests include short-wave infrared system design and high-speed data acquisition.



**Jun Liu**, was born in China, in 1973. He received the B.S. degree in mechanical engineering from North University of China, Taiyuan, China, in 1997, and M.S. degree in mechanical engineering from Xidian University, Xian, China, in 2007.

He is currently a Research Assistant with the Shanghai Institute of Technical Physics, Chinese Academy of Sciences, Beijing, China. His research interests include aerospace optoelectronic instrument design.





**Changxing Zhang**, was born in China, in 1988. He received the B.S. and M.S. degrees in remote sensing of resources and environments from China University of Geosciences, Wuhan, China, in 2011 and 2014.

He is currently an Electronic Engineer with the Shanghai Institute of Technical Physics, Chinese Academy of Sciences, Beijing, China. His research interests include the processing and application of hyperspectral and infrared data.



**Shengwei Wang**, was born in China. He received the B.S. in optical information from University of Shanghai for Science and Technology, Shanghai, China, in 2006.

He is currently an Electronic Engineer with the Shanghai Institute of Technical Physics, Chinese Academy of Sciences, Beijing, China. His research interests include hyperspectral imaging system design and the electronics system design.